Supplementary Information for

Identification of Ni₃Fe Alloy as a Candidate Catalyst for Quinoline Selective Hydrogenation with Computations

Zhaochun He[a,b,c,†], Yonghua Liu[b,c,†], Tao Wang[a,b,c,*]

[a] Division of Solar Energy Conversion and Catalysis at Westlake University, Zhejiang Baima Lake Laboratory Co., Ltd., Hangzhou 310000, Zhejiang, China.

[b] Center of Artificial Photosynthesis for Solar Fuels and Department of Chemistry, School of Science and Research Center for Industries of the Future, Westlake University, 600 Dunyu Road, Hangzhou 310030, Zhejiang Province, China.

[c] Institute of Natural Sciences, Westlake Institute for Advanced Study, 18 Shilongshan Road, Hangzhou 310024, Zhejiang Province, China.

[†] These authors contributed equally to this work.

Email: twang@westlake.edu.cn

1. Computational details

2. Microkinetic modeling details

Fig. S1 The intermediates in QL hydrogenation reaction without considering the alternating hydrogenation process of benzene and nitrogen heterocycle.

Fig. S2 The theoretically fitted Sabatier volcano of QL hydrogenation activity.

Fig. S3 Top and side views of QL adsorption configuration on 18 bimetallic catalysts (111) surface and hydrogen atom was represented by white stick.

Fig. S4 Top and side views of the initial, transition and final states of the optimal pathway of QL hydrogenation on the $Ni_3Fe(111)$ surface.

Fig. S5 The potential energy profile of QL hydrogenation on bimetallic catalyst $AuPd_3(111)$ surface at 353.15 K with free energy corrections.

Table S1 The calculated binding energies (E_{QL}, eV) and measured turnover frequency (TOF) of QL on Au, Pd and Au_xPd_y bimetallic catalysts.

Table S2 The calculated binding energies (E_{QL}, eV) of QL on bimetallic catalysts (111) surface (ratio = 1:3, 1:1, 3:1) and formation energies (E_f, eV) of bimetallic catalysts.

Table S3 Free energy barrier (Ga, eV) and hydrogenation sites for all steps of QL hydrogenation to py-THQL and H_2 dissociation on $Ni_3Fe(111)$ surface at 353.15K.

1. Computational details

All DFT calculations are implemented in the Vienna Ab-initio simulation package (VASP)[1]. The BEEF-vdW functional[2] was used to describe the exchange-correlation contribution to the electronic energy due to the accuracy of describing the adsorption proprieties of adsorbates on transition-metal surfaces. We employed the periodic slab models to simulate surfaces to calculate adsorption energy and the hydrogenation process. The most stable (111) surface for FCC and (110) surface for BCC was chosen for the mechanistic study. The (111) and (110) surfaces were simulated using 4-layered (4×4) supercells constrained bottom two layers and relaxed top two layers to model the substrate and surface of the catalyst, using 15Å of vacuum space in the periodically repeated slabs to eliminate the effects between the surfaces. The cutoff energy was set to 400 eV to obtain accurate energy. All calculations were done when the force and energy difference were smaller than 0.05 eV/A and 10^{-4} eV, respectively. The binding energies of QL were defined as $E_{QL} = E_{(QL/surface)} - E_{(surface)} - E_{(QL, g)}$, where $E_{(QL/surface)}$, $E_{(surface)}$, and $E_{(QL, g)}$ are the total electronic energies of QL adsorbed on bimetallic catalysts surfaces, clean surfaces, and QL molecular in the gas phase, respectively. The formation energy of bimetallic alloys was defined as $E_f = \frac{[E(A_xB_y) - xE_A - yE_B]}{x+y}$, where $E(A_xB_y)$, E_A and E_B are the total energy of alloy bulk, the energy of A atom and B atom from metal bulk, respectively. The transition states of each hydrogenation step were located by the climbing image nudged elastic band (CINEB) method.[3] The Gibbs free energy barriers (G_a) were defined as the $G_a = G_{(TS)} - G_{(IS)}$, where $G_{(IS)}$, $G_{(TS)}$ are the total free energies of initial states (IS) and transition state (TS) of each hydrogenation steps, respectively. All transition states are analyzed by frequency calculations with only one imaginary frequency. The thermodynamic correction of adsorbents and gas is based on Harmonic and ideal gas approximations as implemented in ASE[4]. The Gibbs free energy was defined as $G = E + E_{ZPE} - TS$, where E, E_{ZPE}, T, and S are the total energies of species absorbed on the surface calculated by DFT calculation, zero-point energy, temperature, and entropy.

2. Microkinetic modeling details

In microkinetic model, a reaction network comprises a set of elementary reactions. According to the transition state (TS) theory, the forward and reverse rate constant of an elementary reaction equals to

$$k^{f/r} = \frac{k_B T}{h} e^{-E_a/k_B T}$$

where k_B is Boltzmann constant, T is the temperature, h is Plank constant and E_a is the activation energy of this elementary step. Then, the rate of this elementary reaction can be written as

$$r_i = k_i^f \prod_m \theta_{im} \prod_m p_{im} - k_i^r \prod_n \theta_{in} \prod_n p_{in}$$

where $\theta_{im/in}$ is the coverage of surface species m (reactant) or n (product), $p_{im/in}$ is the pressure of gas m (reactant) or n (product) for each elementary reaction step i. Here, the collision probability is expressed as the product of the reactants' coverage or pressure, utilizing mean-field approximation.

The coverage of species is determined by the state reached by the reaction network at equilibrium. When the network reaches steady state, the coverage of all adsorbates remains constant over time. This allows us to derive a set of nonlinear equations:

$$\frac{\partial \theta_m}{\partial t} = 0, \sum_i \theta_m = 1$$

where θ_m is the coverage of the surface species m, the derivative of coverage $(\partial \theta_m / \partial t)$ is the sum of the elementary reactions' rates, m is among the reactants and products. These equations can be solved by iteratively applying the Jacobi matrix. The turnover frequency (TOF) of the products can be obtained from the rate expressions and the solved coverage.

The computational process is carried out by the Catalysis Microkinetic Analysis Package (CatMAP)[5]. The code has been enhanced for improved accuracy and completeness of solutions. In this study, the descriptors are temperature and the logarithm of pressure. The TOF data in **Figure 3 (A-B)** are calculated at a fixed gas phase composition (1/3 QL and 2/3 H_2). The temperature ranges from 200 K to 800 K, and the pressure ranges from 0.1 bar to 1000 bar. To account for temperature variations, the free energies of QL and py-THQL are corrected using the partition function of the ideal gas, based on the optimized gas structure, free energy, and frequencies obtained from DFT. The free energies of adsorbates and transition states are corrected using the partition function of the harmonic adsorbate, considering the free energy and frequencies provided by DFT.

The total reaction network of the MKM on $Ni_3Fe(111)$ surface and $AuPd_3(111)$ surface includes the following elementary reactions:

(1) $H_2\_g + 2* \leftrightarrow 2H*$

(2) $C_9H_7N\_g + * \leftrightarrow C_9H_7N*$

(3) $C_9H_7N^* + H^* \leftrightarrow C_9H_7N\text{-}H^* + * \leftrightarrow C_9H_8N^* + *$

(4) $C_9H_8N^* + H^* \leftrightarrow C_9H_8N\text{-}H^* + * \leftrightarrow C_9H_9N^* + *$

(5) $C_9H_9N^* + H^* \leftrightarrow C_9H_9N\text{-}H^* + * \leftrightarrow C_9H_{10}N^* + *$

(6) $C_9H_{10}N^* + H^* \leftrightarrow C_9H_{10}N\text{-}H^* + * \leftrightarrow C_9H_{11}N^* + *$

(7) $C_9H_{11}N^* \leftrightarrow C_9H_{11}N\_g + *$

where the g denotes gas, and * denotes the active sites. The adsorbate-adsorbate interaction is not considered in this model.
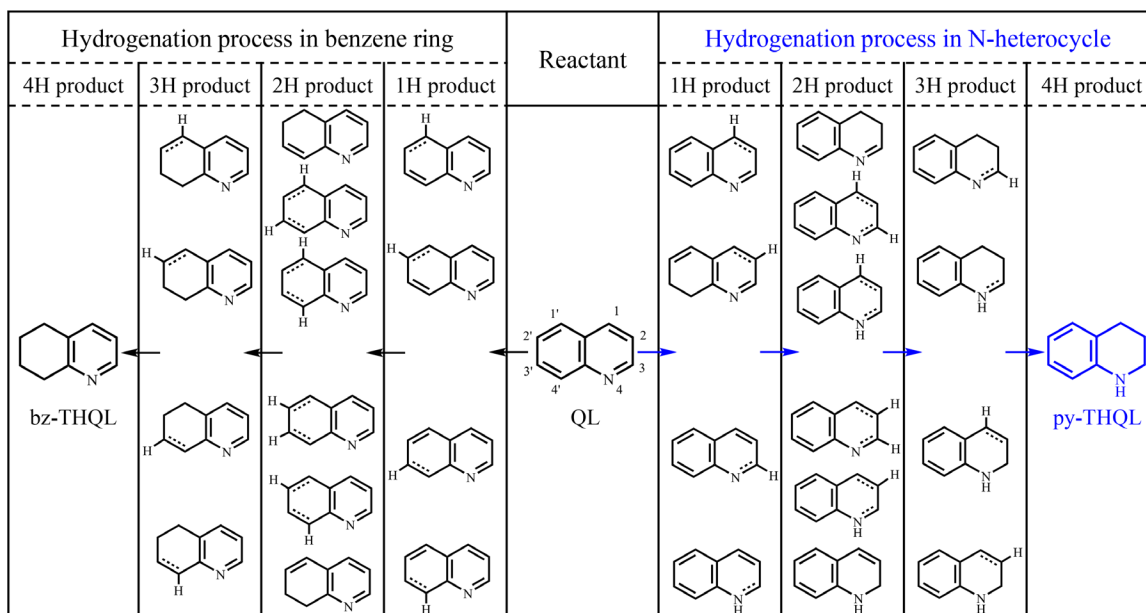
Fig. S1 The intermediates in QL hydrogenation reaction without considering the alternating hydrogenation process of benzene and N-heterocycle.
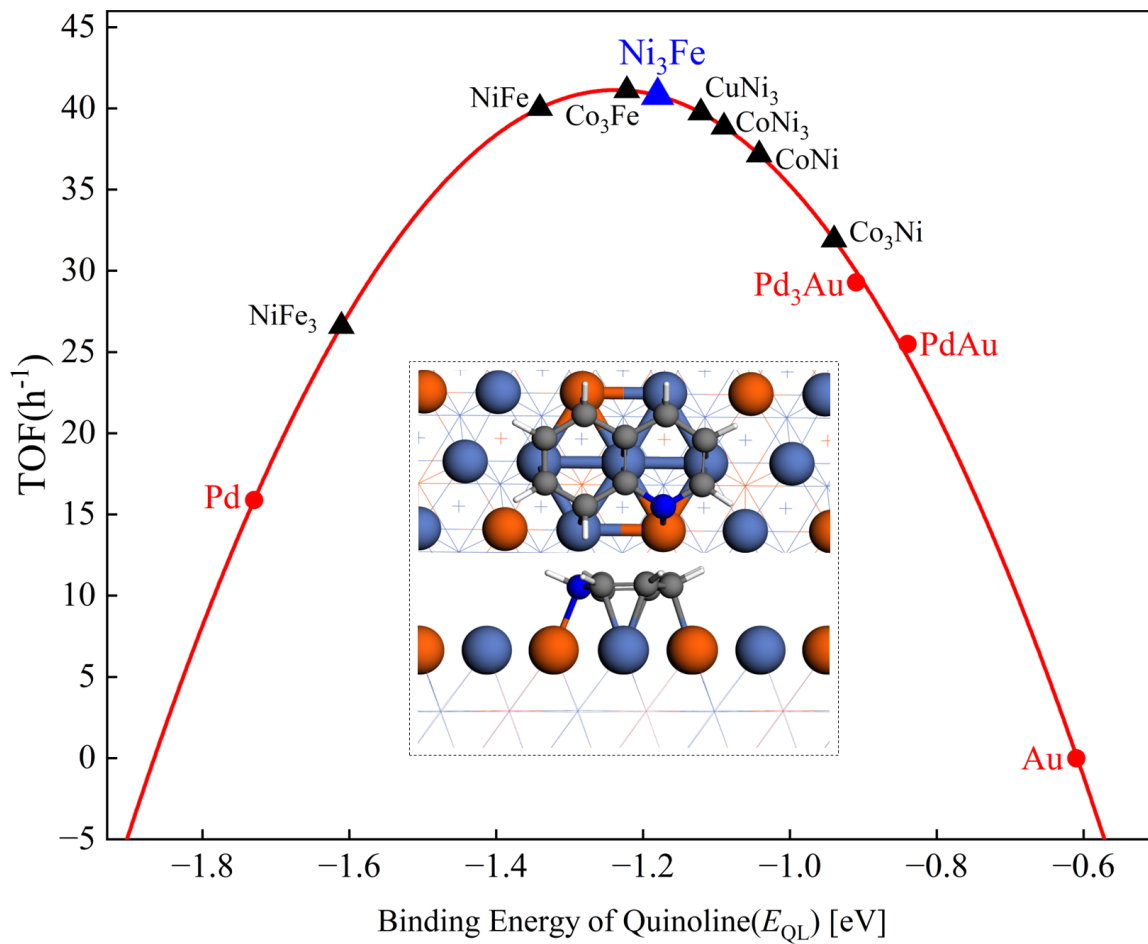
Fig. S2 The theoretically fitted Sabatier volcano of QL hydrogenation activity.
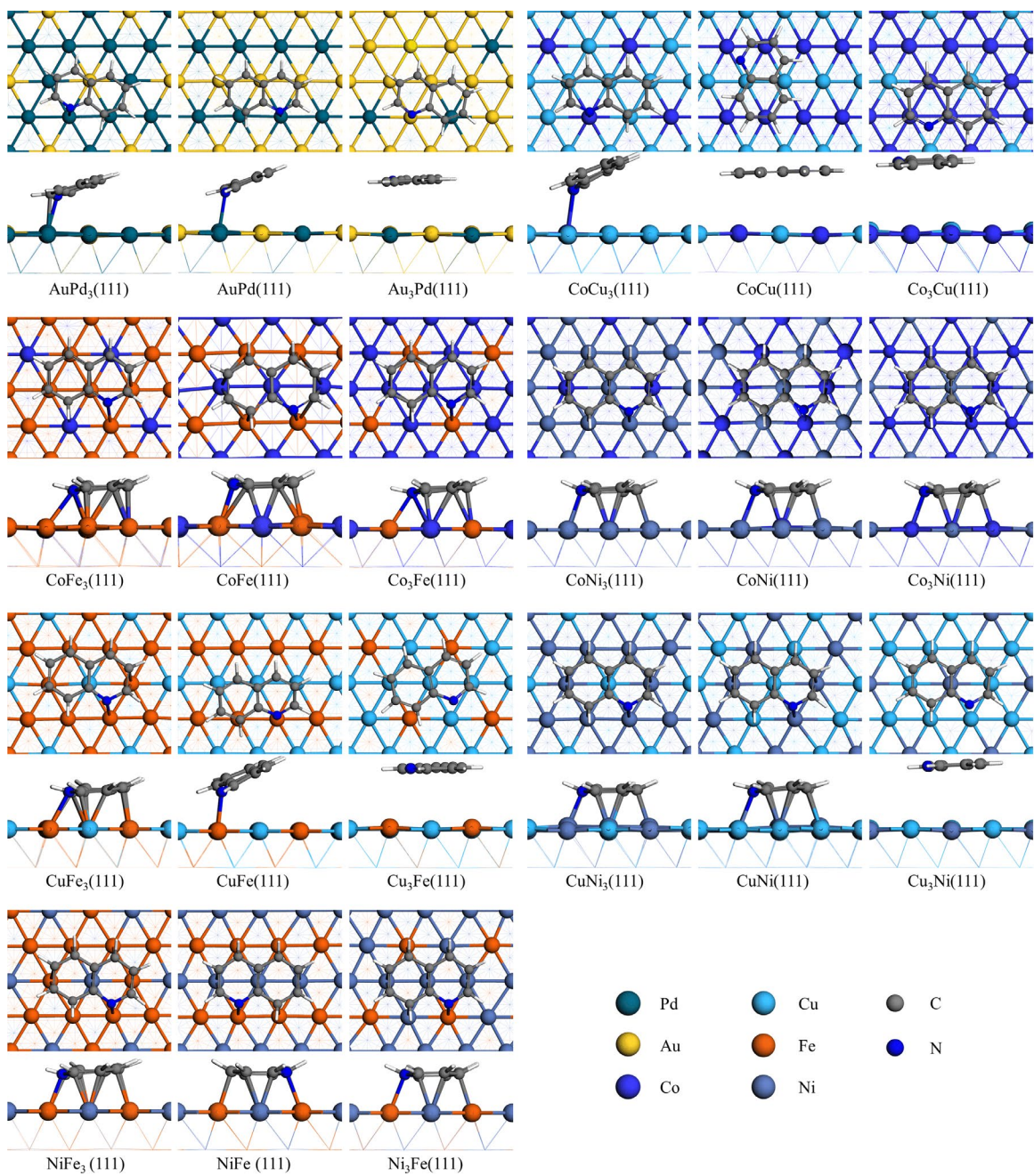
Fig. S3 Top and side views of QL adsorption configuration on 18 bimetallic catalysts (111) surface and hydrogen atom was represented by white stick.
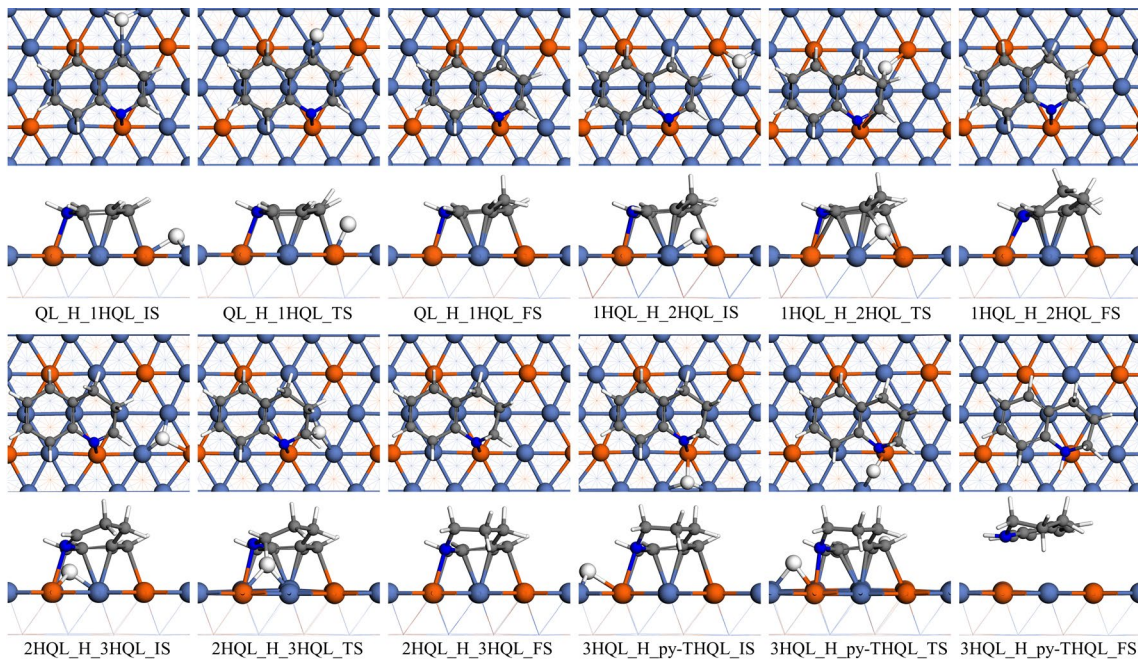
QL_H_1HQL_IS   QL_H_1HQL_TS   QL_H_1HQL_FS   1HQL_H_2HQL_IS   1HQL_H_2HQL_TS   1HQL_H_2HQL_FS

2HQL_H_3HQL_IS   2HQL_H_3HQL_TS   2HQL_H_3HQL_FS   3HQL_H_py-THQL_IS   3HQL_H_py-THQL_TS   3HQL_H_py-THQL_FS

Fig. S4 Top and side views of the initial, transition and final states of the optimal pathway of QL hydrogenation on the Ni$_3$Fe(111) surface.
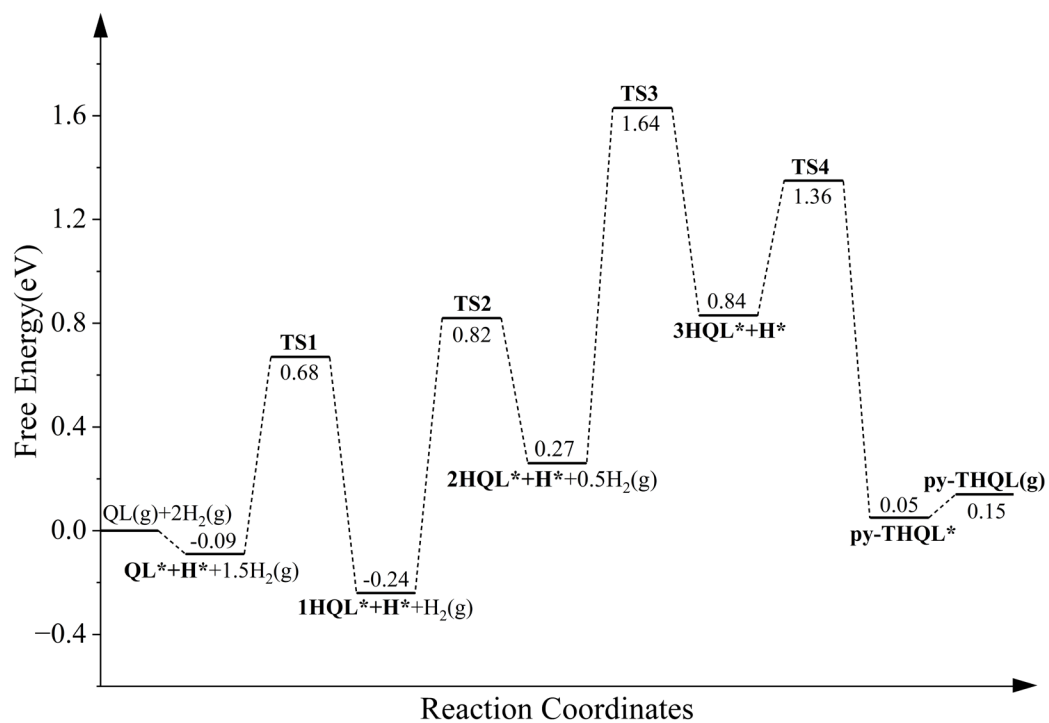
Fig. S5 The potential energy profile of QL hydrogenation on bimetallic catalyst $AuPd_3(111)$ surface at 353.15 K with free energy corrections. (Caption: The data on the potential energy profile of $AuPd_3$ is obtained by reproducing the work of Cui and Wang[6])

Table S1 The calculated binding energies (E_{QL}, eV) and measured turnover frequency (TOF) of QL on Au, Pd and Au_xPd_y bimetallic catalysts. (The data of TOF of QL to py-TQHL on Au_xPd_y catalyst are taken from our own work in ref [6].)

Catalyst	E_{QL} (eV)	TOF (s^{-1})
Pd	-1.73	15.9
AuPd$_3$	-0.91	29.3
AuPd	-0.84	25.5
Au	-0.61	0

Table S2 The calculated binding energies (E_{QL}, eV) of QL on bimetallic catalysts (111) surface (ratio = 1:3, 1:1, 3:1) and formation energies (E_f, eV/atom) of bimetallic catalysts.

Catalyst	E_{QL} (eV)	E_f (eV/atom)
$AuPd_3$	-0.91	-0.057
AuPd	-0.84	-0.087
Au_3Pd	-0.70	-0.079
$CoCu_3$	-0.70	0.180
CoCu	-0.62	0.172
Co_3Cu	-0.61	0.120
$CoFe_3$	-1.99	0.082
CoFe	-2.01	-0.080
Co_3Fe	-1.22	-0.005
$CoNi_3$	-1.09	0.010
CoNi	-1.04	-0.004
Co_3Ni	-0.94	-0.009
$CuFe_3$	-1.58	0.123
CuFe	-0.68	0.150
Cu_3Fe	-0.47	0.217
$CuNi_3$	-1.12	0.033
CuNi	-0.82	0.046
Cu_3Ni	-0.59	0.012
$NiFe_3$	-1.61	0.032
NiFe	-1.34	-0.072
Ni_3Fe	-1.18	-0.090

Table S3 Free energy barrier (Ga, eV) and hydrogenation sites for all steps of QL hydrogenation to py-THQL and H_2 dissociation on $Ni_3Fe(111)$ surface at 353.15K.

Process	Reaction	Ga/eV	Hydrogenation Site
1H	QL* + H* → 1HQL-1* + *	1.03	C_1
1H	QL* + H* → 1HQL-2* + *	1.34	C_2
1H	QL* + H* → 1HQL-3* + *	1.26	C_3
1H	QL* + H* → 1HQL-4* + *	1.25	N_4
1H	QL* + H* → 1HQL-1'*+ *	1.15	$C_{1'}$
1H	QL* + H* → 1HQL-2'*+ *	1.24	$C_{2'}$
1H	QL* + H* → 1HQL-3'*+ *	1.15	$C_{3'}$
1H	QL* + H* → 1HQL-4'*+ *	1.12	$C_{4'}$
2H	1HQL-1* + H* → 2HQL-2* + *	0.87	C_2
2H	1HQL-1* + H* → 2HQL-3* + *	1.37	C_3
2H	1HQL-1* + H* → 2HQL-4* + *	1.20	N_4
2H	1HQL-1* + H* → 2HQL-1'* + *	1.13	$C_{1'}$
2H	1HQL-1* + H* → 2HQL-2'* + *	1.25	$C_{2'}$
2H	1HQL-1* + H* → 2HQL-3'* + *	1.46	$C_{3'}$
2H	1HQL-1* + H* → 2HQL-4'* + *	1.08	$C_{4'}$
3H	2HQL-2* + H* → 3HQL-3* + *	0.88	C_3
3H	2HQL-2* + H* → 3HQL-4* + *	1.39	N_4
3H	2HQL-2* + H* → 3HQL-1'* + *	1.39	$C_{1'}$
3H	2HQL-2* + H* → 3HQL-2'* + *	1.15	$C_{2'}$
3H	2HQL-2* + H* → 3HQL-3'* + *	1.25	$C_{3'}$
3H	2HQL-2* + H* → 3HQL-4'* + *	1.10	$C_{4'}$
4H	3HQL-3* + H* → py-THQL* + *	1.05	N_4
4H	3HQL-3* + H* → 4HQL-1'* + *	1.31	$C_{1'}$
4H	3HQL-3* + H* → 4HQL-2'* + *	1.28	$C_{2'}$
4H	3HQL-3* + H* → 4HQL-3'* + *	1.22	$C_{3'}$
4H	3HQL-3* + H* → 4HQL-4'* + *	1.09	$C_{4'}$
H_2 dissociation	H_2+ 2* → H* + H*	0.09	Ni

REFERENCES

1   G. Kresse and J. Furthmüller, *Comput. Mater. Sci.*, 1996, **6**, 15-50.

2   J. Wellendorff, K. T. Lundgaard, A. Møgelhøj, V. Petzold, D. D. Landis, J. K. Nørskov, T. Bligaard and K. W. Jacobsen, *Phys. Rev. B*, 2012, **85**, 235149.

3   G. Henkelman, B. P. Uberuaga and H. Jónsson, *J. Chem. Phys.*, 2000, **113**, 9901-9904.

4   S. R. Bahn and K. W. Jacobsen, *Comput. Sci. Eng.*, 2002, **4**, 56-66.

5   A. J. Medford, C. Shi, M. J. Hoffmann, A. C. Lausche, S. R. Fitzgibbon, T. Bligaard and J. K. Nørskov, *Catal. Lett.*, 2015, **145**, 794-807.

6   X.-J. Cui, Z.-J. Huang, A. P. van Muyden, Z.-F. Fei, T. Wang and P. J. Dyson, *Sci. Adv.*, 2020, **6**, eabb3831.